



ELSEVIER

Contents lists available at [ScienceDirect](https://www.sciencedirect.com)

Urban Climate

journal homepage: www.elsevier.com/locate/uclim

Automated mapping process of frontal area and thermal potential indexes: GIS algorithm development and implementation

Ana Paula Oliveira Favretto^a, Léa Cristina Lucas de Souza^a, Daniel Souto Rodrigues^{b,*}

^a Federal University of São Carlos (UFSCar), Centre for exact science and technology (CCET), Urban Engineering Graduate Program (PPGEU), Rodovia Washington Luis, km 235, São Carlos, São Paulo Zip-Code: 13565-905, Brazil

^b University of Minho, Centre for Territory, Environment and Construction (CTAC), Portugal

ARTICLE INFO

Keywords:

Urban thermal comfort
Urban Heat Island
Frontal Area Index
GIS
Wind route

ABSTRACT

The impacts of urban areas on microclimate conditions are well-known and highlight the importance of climatological guided urban planning. The growth and evolution of Geographic Information Systems (GIS) have set a backdrop for implementing strategies to apply urban climatological knowledge in planning daily practice. This research brings algorithms to automate the Frontal Area Index (FAI) and Thermal Potential Index (TPI) mapping process. This type of algorithms type facilitates the extraction of detailed spatial information for the decision-making process, making it highly relevant for urban planning and management. Their calculation method is implemented as ESRI © ArcGIS Pro embedded Python Stand Alone Script Tools, using the Python ArcPy library to access the ArcGIS geoprocessing functions. The algorithms are described in detail, allowing their implementation in other GIS platforms. The output maps allow the urban thermal conditions and morphology assessment. The findings from this research may substantially contribute both to the advance in the urban climatology scientific field and to guide urban planners' and managers' practical decision making.

1. Introduction

Incorporating urban climatology knowledge to guide urban planning is key to achieving good thermal comfort levels in cities, especially because environmental thermal conditions are directly and indirectly connected with the population health and well-being (Arifwidodo and Chandrasiri, 2020; Deschenes, 2014; Kravchenko et al., 2013; Marchetti et al., 2016; McGeehin and Mirabelli, 2001; Omonijo, 2017; Paz et al., 2016; Wright et al., 2014; Yao-Dong et al., 2013; Zhang et al., 2018). Even when climate change resulting from the effects of global warming is disregarded, urban expansion is related to an increase in temperature (Doan et al., 2016; Georgescu et al., 2014; Yang et al., 2021a). In addition to strategies aimed at mitigating climate change on a global scale (i.e., mainly aimed at controlling the emission of pollutants, deforestation, etc.), they must be devised addressing the relationship between the development of cities and their climate impacts (Jabareen, 2015).

Urban climatology is a mature science field that provides an abundant and rich amount of information on climate phenomena in urban areas (Arnfield, 2003; Hebbert, 2014; Hebbert and Jankovic, 2013; Mills, 2014). However, there are technical, legal, political

* Corresponding author at: University of Minho, Centre for Territory, Environment and Construction (CTAC), Campus de Azurém, 4800-058 Guimarães, Portugal.

E-mail address: dsr@civil.uminho.pt (D.S. Rodrigues).

<https://doi.org/10.1016/j.uclim.2023.101799>

Received 8 December 2021; Received in revised form 14 December 2023; Accepted 28 December 2023

Available online 12 January 2024

2212-0955/© 2024 The Authors. Published by Elsevier B.V. This is an open access article under the CC BY-NC license (<http://creativecommons.org/licenses/by-nc/4.0/>).

and economic barriers to translating this knowledge into science application (Hebbert and Mackillop, 2013). On the technical matter, Ren et al. (2013) discuss the difficulty of the translation between scientists and city planners working languages, pointing out to the planners and scientists educational background differences, that leads to different levels of the scientific equations comprehension and its translation into meaningful language for policy application. Hebbert (2014) indicates that this gap may now be addressed by taking advantage of the computer technology advances, such as Geographic Information Systems (GIS), to develop and provide tools that may offer support to incorporate climate concerns during the urban planning stages. Considering this point of view, this paper provides a useful tool to help on filling this gap, by bringing algorithms to automate important climatological urban indices.

Simplified urban climate analysis methods expedite and reduce computational costs. In addition, they reduce the modelling input and output complexity, demanding less computational expertise from the users and, consequently, benefiting urban planners and city managers throughout the urban design and planning process. Urban climatology offers knowledge – e.g., the relationship between urban morphology and ventilation patterns and the relationship between ground cover materials (asphalt, concrete, vegetation, water surfaces, etc.) and the microclimate temperature - that could be used to implement such simplified assessment methods.

The relationship between urban morphology and ventilation patterns is addressed by many authors using different methods and techniques. Fan et al. (2017) considered urban morphology aspects to formulate a new street air-wind index to evaluate the pedestrian-level air quality and wind comfort. He et al. (2022) investigated the relationship of irregular breezeway morphologies and the pedestrian-level wind performance. J. Li et al. (2022) explored the correlation between an urban morphological parameter (the sky view factor) and the ventilation conditions. Liu et al. (2022) considered urban morphological parameters while investigating multiple factors that are closely related to urban ventilation and developed a method for assessing urban wind environment using multi-source data. Palusci et al. (2022) used CFD simulation results to develop linear regression models for predicting areas vulnerable to poor air conditions. Also, the authors provide a review of morphological parameters used for generic studies about the relationship between urban geometries and urban ventilation. Du et al. (2022) considered several urban morphology indices (such as Frontal Area Index (FAI), plan area ratio, effective height, façade area ratio, mean building height, etc.) while reviewing factors that impact the urban thermal and wind environment. The FAI index is particularly highlighted in our work, for its simplified and quickly way of considering urban impact on climate.

The FAI corresponds to the area of buildings' windward facade projection on a plane normal facing the wind direction, minus possible duplicated areas caused by projection overlaps, divided by the floor area containing projected buildings (Wong et al., 2010). It describes some aspects of urban morphology regarding, among others, wind permeability. Y. Liu et al. (2020) assessed the correlation between 8 spatial morphological parameters with the near-surface wind speed in Beijing, mentioning the FAI among the three indexes that shows the highest contribution rates to the Wind Speed Ratio change. Yang et al. (2021b) used this index to categorize the ventilation conditions in 31 cities of China and concluded that its influence on urban ventilation performance is an effective factor towards regulating the urban thermal environment. Also, FAI has been used in the literature to predict urban wind routes in a simplified way (L. Chen and Ng, 2011; Gál and Unger, 2009; Hsieh and Huang, 2016; Peng et al., 2017; Wong et al., 2010). These predicted routes have been compared and validated, in the literature, against predictions made with more sophisticated models, such as wind tunnel tests and CFD simulations. Based on concepts validated by these works, the main aspect that differentiates the present research was the development and disclosure of a vector-based FAI calculation algorithm, rather than using raster data or conducting specific case study mappings.

The relationship between ground cover materials (e.g. asphalt, concrete, vegetation, water surfaces, etc.) and the microclimate temperature is also addressed in the literature (Acero and González-Asensio, 2018; Alchapar et al., 2017; Banerjee et al., 2022; Doulos et al., 2004; Faragallah and Ragheb, 2022; Hsieh and Huang, 2016; Igun and Williams, 2018; Kleerekoper et al., 2012; Moazzam et al., 2022; Saaroni et al., 2000; Smith et al., 2023; Tun and Mg, 2020). An example of simplified assessment method regarding this matter is presented by Hsieh and Huang (2016) which developed an interesting model to map ground cover materials' heating and cooling thermal potential. In short, this mapping technique begins by classifying the ground cover surface in three groups: (i) heating, (ii) cooling, and (iii) neutral. Then, considering calculation cells from a regular grid, the area of the ground surface occupied by group i and ii is calculated. Positive values are assigned to the heating areas, and cooling areas receive negative values. These areas are summed, and each calculation cell receives a value, which are positive if the cell has mostly heating potential, null for neutral potential, and negative for cooling potentials. Our proposed calculation routines consider material's thermal performance differences through an automated method for calculating the proposed Thermal Potential Index (TPI) of ground cover materials. The TPI, based on Hsieh and Huang's (2016) heating and cooling mapping, distinguishes itself by utilizing an adimensional unit instead of the material ground cover area. Moreover, unlike focusing on a specific study case, our approach develops and discloses calculation routines to automate both the index mapping and computation.

Many different methods have also been used to assess the relationship between urban morphology and land and/or air surface temperature. For example, Xu et al. (2019) based their assessment on mobile measurement; Guo et al. (2023) used tree ensemble algorithm like the random forest regression; Yin et al. (2022) the Multi-access Geographically Weighted Regression Model, S. Chen et al. (2023) studied the effect of urban morphological variables on urban canopy temperature through regression analysis; Y. Chen et al. (2023) used the XGBoost model to study the spatial distribution characteristics of land surface temperature (LST) and its relationship with urban spatial form (USF) at different grid scales; Han et al. (2023) used a random forest regression model to quantify the effects of 2D/3D building indicators on LST; Kotharkar et al. (2023) calculated statistical correlations to assess the hourly influence of morphological parameters with symmetrically distributed data of micrometeorological indicators; H. Li et al. (2021) studied the seasonal correlation of the 3DBF factors with LST; Shi and Zhang (2022) used fixed measurements to investigate the effects of urban morphological indicators on the urban heat island intensity (UHII); to associate the urban morphologies with air temperature increment, Yuan et al. (2020) conducted a regression analysis using CFD simulation result, and developed also a GIS

modelling-mapping tool; J. Zhang et al. (2022) applied an Envi-met model to assess the influence of urban morphology on the mean radiant temperature (MRT) and the physiological equivalent temperature (PET).

Embedding simplified analysis methods into GIS, with automatic calculation and mapping processes, enables the large-scale observation and recording of the urban climatological potential. This provides urban planners and managers with a simple, powerful and expedite way to consider such aspects conjointly with other multiple information layers. While many authors have utilized this approach to conduct valuable case studies, few papers have focused on developing and disclosing the implemented algorithms (Back et al., 2023; Lindberg et al., 2018; Nakata-Osaki et al., 2018; Touati et al., 2020).

Considering the importance of useful climate guided tools for urban planning and the relevance of its availability for urban management, the purpose of this paper is to offer a practical and simple model to fulfil gaps, by disclosing algorithms that may easily be implemented for urban climate analysis. The novelty of this proposal lies not only on this disclosing purpose, but also on the possibility of simultaneously calculating two important urban climate indexes aiming a day-to-day urban planning and management. This paper presents newly developed calculation routines, based on vector attributes within a GIS, to automatize the calculation of the FAI and the ground cover material Thermal Potential Index (TPI), which is a new index approach based on an urban ground surface map model applied by Hsieh and Huang's (2016) on a study area. Moreover, as a way to confirm the developed automation algorithm operability, these calculation routines are implemented as Python Script Tools¹ in ArcGIS Pro. The resultant models are easy to use, allowing urban planning professionals and city managers to assess and compare the wind patterns and microclimate thermal scenarios arising from different urban intervention strategies. Furthermore, the findings presented in this paper contribute to the advance of scientific knowledge as researchers could both use the implemented Script Tools to enlarge microclimate study cases and use the calculation routine description to implement similar tools within other GIS platforms and computer languages.

2. Method

The overall approach encompasses the development of subroutines embedded into a computational model calculation algorithm focusing on the urban thermal environment. The final model receives urban spatial and ground surface input data and provides wind permeability and surface thermal potential analytic maps.

Wind permeability issues are considered based on the FAI values (Hsieh and Huang, 2016), and surface thermal potential issues are considered based on the proposed TPI. Both indexes are computed within a square-shaped grid positioned orthogonally to wind direction. The user of the final model is allowed to define the calculation grid resolution, wind direction angle and, optionally, a weighted value for each groundcover material thermal potential.

The calculation subroutine algorithms are implemented in Python as stand-alone scripts tools embedded in an ArcGIS Pro toolbox. The model development is divided into four main steps, including procedures to: (a) process the user input data, (b) create the calculation grid, (c) calculate and map the FAI, and (d) calculate and map the ground cover surface TPI. These steps are described in detail hereinafter.

2.1. Processing user input data

The proposed algorithms for conducting FAI and TPI analyses require six input data, five mandatory and one optional (Table A.1, see appendix). These inputs are: (i) assessment area boundary, (ii) cell size dimension, (iii) wind direction, (iv) buildings, (v) ground cover surfaces, and (vi - optional) ground cover surface weight.

2.1.1. Assessment area boundary

The assessment area boundary is defined by a single polygon feature that delimits the area to be analysed. This polygon provides the coordinates of two key points: its centroid and the vertex furthest from the centroid. The distance between these two points corresponds to the radius (r) of the circle inscribed within the assessment area boundary polygon.

2.1.2. Cell size dimension

This input represents the linear dimension of one grid cell side and determines the grid calculation resolution. Users have the flexibility to choose any grid size, but it is mandatory to use the unit of distance in meters.

2.1.3. Wind direction

The wind direction angle input is provided in degrees for user convenience. It starts at the cardinal direction North (0°) and increases along the clockwise direction (East = 90° , South = 180° , West = 270°). The input follows the conventional meteorological quadrant.

2.1.4. Buildings

The Buildings input consists of a feature layer containing polygon features that represent the footprints of buildings within the assessment area. This input necessitates the inclusion of a height attribute, which must be specified in meters and found in a column

¹ Available for download at <https://civil.uminho.pt/planning/dsr/FAITPI/FAITPIToolbox.zip>

labelled ‘H’ within the feature layer attribute table. Additionally, the feature layer must be in the UTM (Universal Transverse Mercator) projection.

2.1.5. Ground cover surfaces

The ground cover surfaces input comprises a feature layer containing polygon features representing different ground cover types. The thermal potential class of each polygon object must be indicated in an attribute field column labelled “THERMAL_MODE”. The ground cover surface data should identify areas of soil with a numeric attribute indicating their thermal potential. The assigned values are as follows: 1 for ground cover with heating potential, 0 for neutral potential, and – 1 for cooling potential.

2.1.6. Ground cover surfaces weight (optional)

The ground cover surface weight is an optional input that allows users to specify the relationship among different ground cover materials’ thermal potential. For instance, a material with a weight value of 2 indicates twice the heating or cooling potential of a material with a weight value of 1. If the user chooses to weigh the TPI by surface material type, a column with weighted values must be added to the feature layer attribute table. The user-defined column title must then be provided as an input data.

2.2. Create calculation polygon grid

The calculation polygon grid consists of a vector grid comprising square polygons that are oriented orthogonally to the user-defined wind direction, covering the entire extent of the assessment area. The creation of the calculation polygon grid involves four key inputs: (i) The coordinates of the centroid point (C) of the assessment area, (ii) the coordinates of the vertex (V) farthest from the centroid, (iii) the user-defined grid cell size in meters, and (iv) the wind direction angle in radians. Fig. 1 depicts the diagram illustrating the generation process of the calculation polygon grid.

Firstly, the distance between the centroid coordinates C and the furthest vertex V is computed, determining the radius r of a circumference that circumscribes the assessment area boundary polygon. Then, to ensure the compatibility of the calculation polygon grid dimensions with the user-defined polygon grid cell size (u), the algorithm verifies whether r is a multiple of u. If the division of r by u results in a remainder, it indicates that r is not a multiple of u. In such cases, r is adjusted to r', which represents the closest and greater multiple of u compared to r.

The subsequent step involves delineating the borders of the calculation grid (refer to Fig. 1). Depending on whether the wind direction angle is orthogonal to the Cartesian axes, two distinct paths may be pursued. If the wind direction angle is orthogonal to the Cartesian axes, the calculation grid’s vertex coordinates are computed using the equations provided in Table A.2 (see appendix).

For non-orthogonal wind direction angles the calculation process involves additional steps. Utilizing the centroid point C coordinate and the wind direction angle reduced to the first quadrant θ' , the coordinates of the intersection points (A, B, D, and E) between the calculation grid border and its inscribed r' radius circumference (Fig. 2) are determined using the equations provided in Table A.3 (see Appendix). Subsequently, the grid border lines are computed using the equations outlined in Table A.4 (see Appendix), along with the coordinates of the polygon cell grid vertices VAB, VBD, VAE, and VDE (Fig. 3), using the Eqs. (A.1), (A.2), (A.3), and (A.4) (see Appendix).

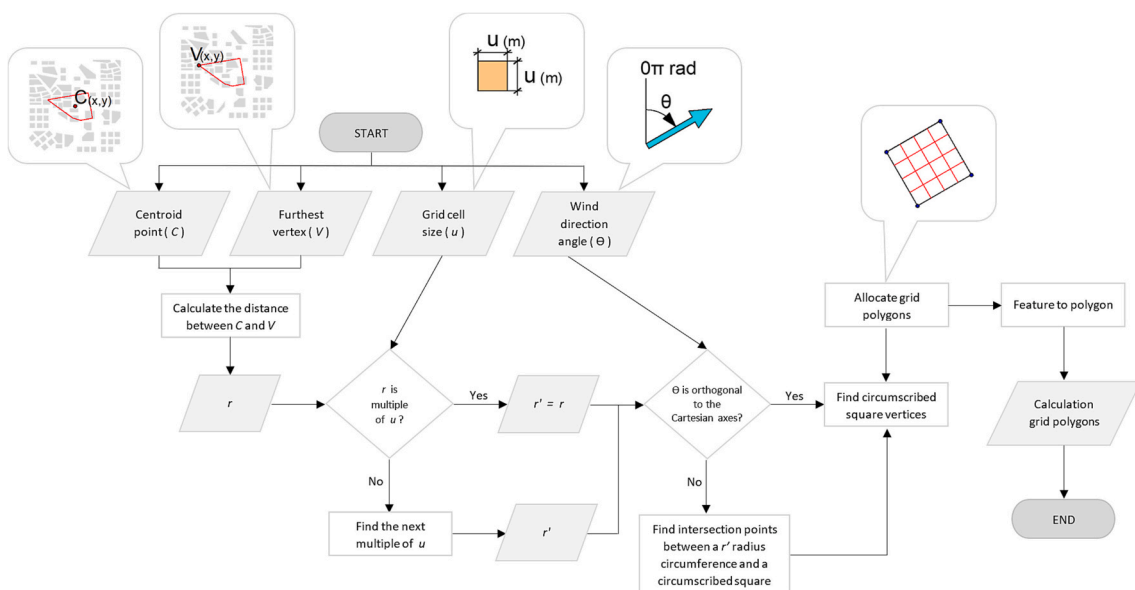


Fig. 1. Calculation grid generation process diagram.

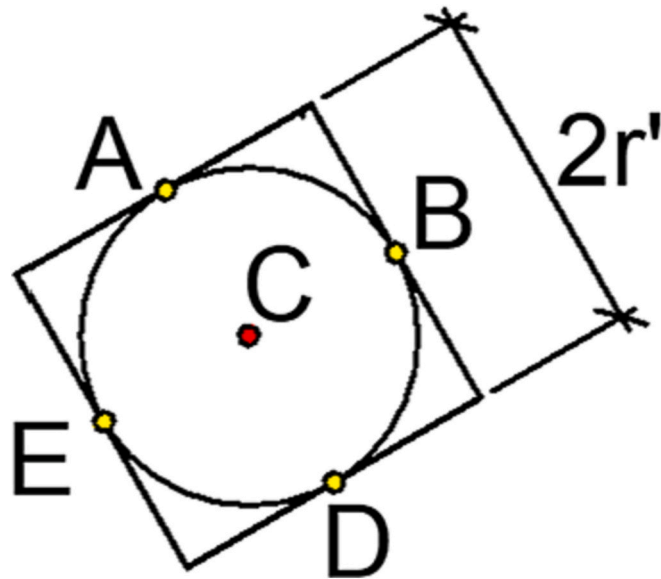


Fig. 2. Intersection points A, B, D and E.

Finally, wind direction perpendicular line segments are interpolated between points V_{AB} and V_{AE}, while wind direction parallel line segments are interpolated between points V_{AB} and V_{BD}. Using the ArcGIS geoprocessing toolbox, feature points are converted to lines, followed by the conversion of line features to polygons. The resulting output is the calculation polygon grid composed of square polygons with dimensions $u \times u$. This grid is orthogonal to the wind direction angle.

2.3. Mapping the Frontal Area Index

To map the Frontal Area Index (FAI), three inputs must be provided: (i) wind direction angle, (ii) calculation polygon grid layer, and (iii) building feature layer. Firstly, the building feature layer is adjusted to ensure that no building polygon overlaps more than one grid cell polygon. Then a series of steps, described hereinafter, are followed for each grid polygon. This involves projecting the buildings' frontal area over a base line, which is normal to the wind direction, and calculating the FAI value for each polygon. An illustration of the overall process is depicted in Fig. 4.

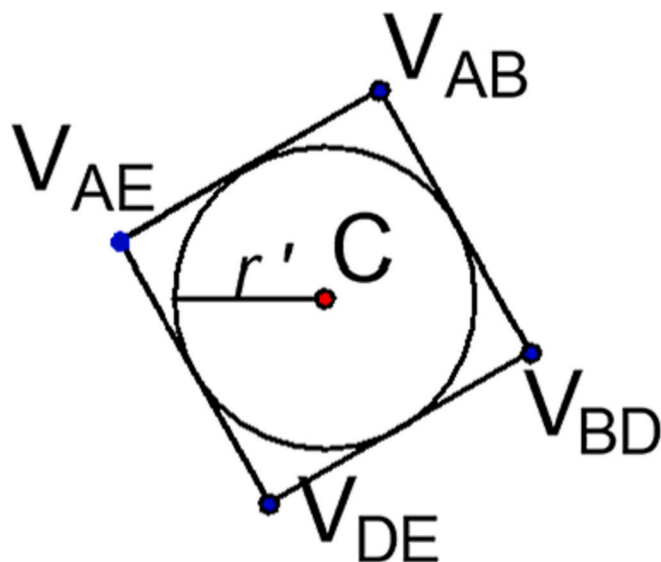


Fig. 3. Polygon cell grid vertices.

2.3.1. Adjusting the building feature layer

This adjustment is a procedure to clip the building feature layer polygons that overlap more than one grid polygon. As a result, a single building that overlaps n grid polygon will be represented by n polygons, one for each grid polygon (Fig. 5).

2.3.2. Defining the buildings' projection base line

For each grid cell polygon, a line segment must be defined to serve as a base for the building frontal area projection. In this research, it is called the buildings' projection base line and must be contained in a normal plane to the wind direction angle (Fig. 6). The definition of the baseline for the building projection is the result of a joint analysis between the coordinates of the grid polygon vertices and the wind direction angle.

Based on the value of θ (wind direction angle), one of four methods is adopted to determine the buildings' projection baseline. These methods require prior knowledge of the coordinates of the grid polygon vertices, which can be easily obtained using the GIS geoprocessing toolbox.

For the cases where $\theta = 0^\circ$ or $\theta = 180^\circ$: the projection base line is delimited by the vertices: (a) with the minimum value on the x axis and maximum value on the y axis, and (b) with the maximum value on the x axis and on the y axis.

For the cases where $\theta = 90^\circ$ or $\theta = 270^\circ$: the projection base line is delimited by the vertices: (a) with the maximum value on both the x and y axis, and (b) with the maximum value on the x axis and the minimum value on the y axis.

For the cases where θ is within odd quadrants (I and III): the projection base line is delimited by the vertices: (a) that show the greater value on the y axis (b) that show the greater value on the x axis.

For the cases where θ is within even quadrants (II and IV): the projection base line is delimited by the vertices: (a) that show the greater value on the y axis (b) that show the lower value on the x axis.

Table A.5 (see Appendix) summarizes the variables and equations to define the buildings' projection base line for the cases where θ is a not an orthogonal angle.

2.3.3. Defining the buildings' vertices projection lines

The buildings' vertices projection lines are wind direction parallel lines which intercept the buildings' polygon vertices and the buildings' projection base line. GIS geoprocessing tools are used to create a feature layer containing sets of vertices points for each building within a calculation grid polygon. Each of these points has an attribute field 'H', which informs the height in meters of the correspondent building. Considering these points coordinates and the angle α_1 , which is given in function of the wind direction angle

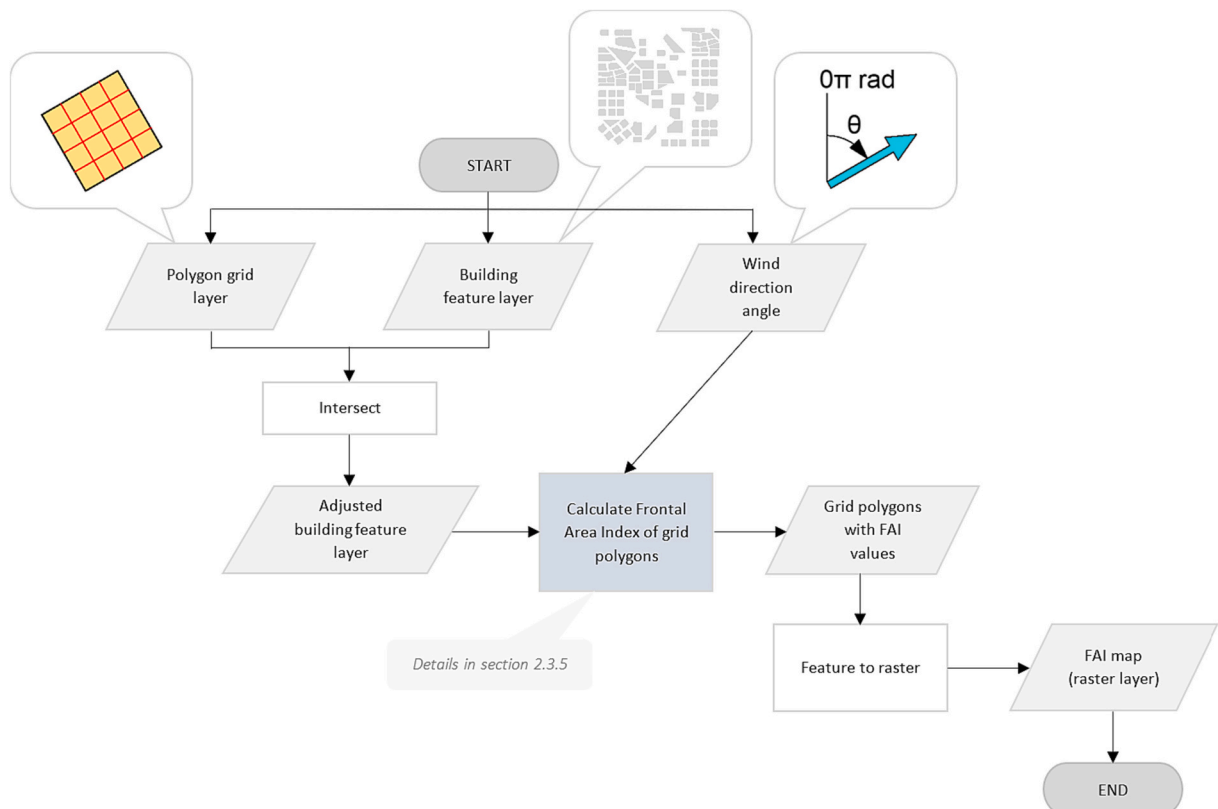


Fig. 4. FAI mapping process diagram.

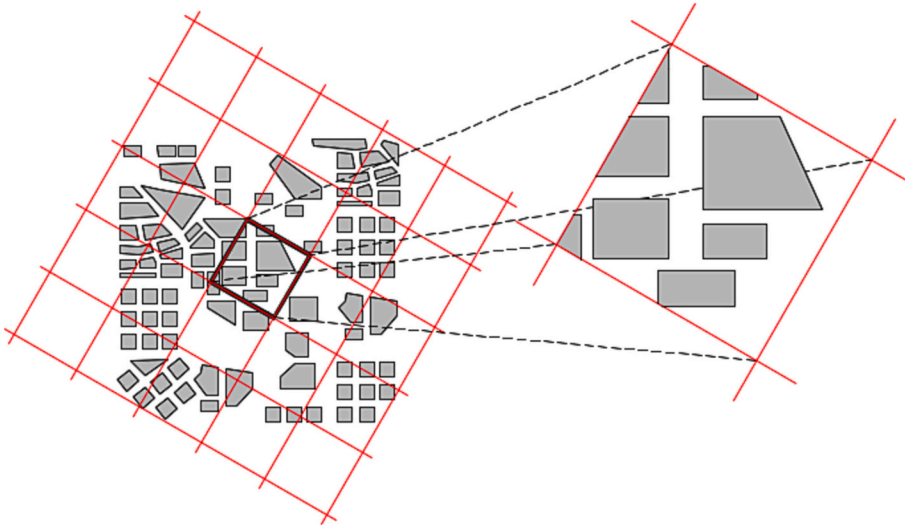


Fig. 5. Building feature layer adjustment.

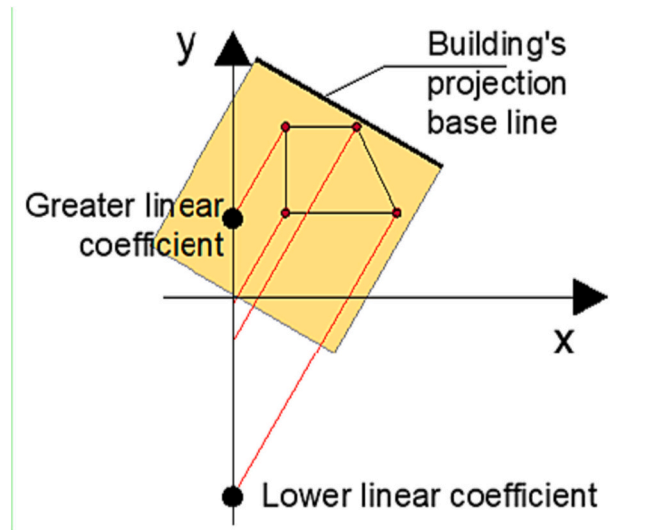


Fig. 6. Building's projection base line.

θ , the line equations are defined. Each line is parallel to the wind direction and intercepts at least one of the building vertices. The θ and α_1 value relationship for each trigonometrical quadrant, and other variables to automate the line equation generation can be found in Table A.6 (see appendix).

2.3.4. Projecting building frontal area

Once the equations of buildings' projection base line and buildings' vertices projection line are known, the building frontal area is projected using the following step:

- Selecting the two vertical buildings' edge lines by considering the line equations that show the greater and lower linear coefficient (Fig. 7 shows an example for the first and third quadrant)
- Using Eq. (1) to find the x axis coordinate of the intersection point between the base line and the vertex projection line

$$x = \frac{n_V - n_{Base}}{m_{Base} - m_V} \tag{1}$$

Where:

n_V is the vertex projection line linear coefficient.

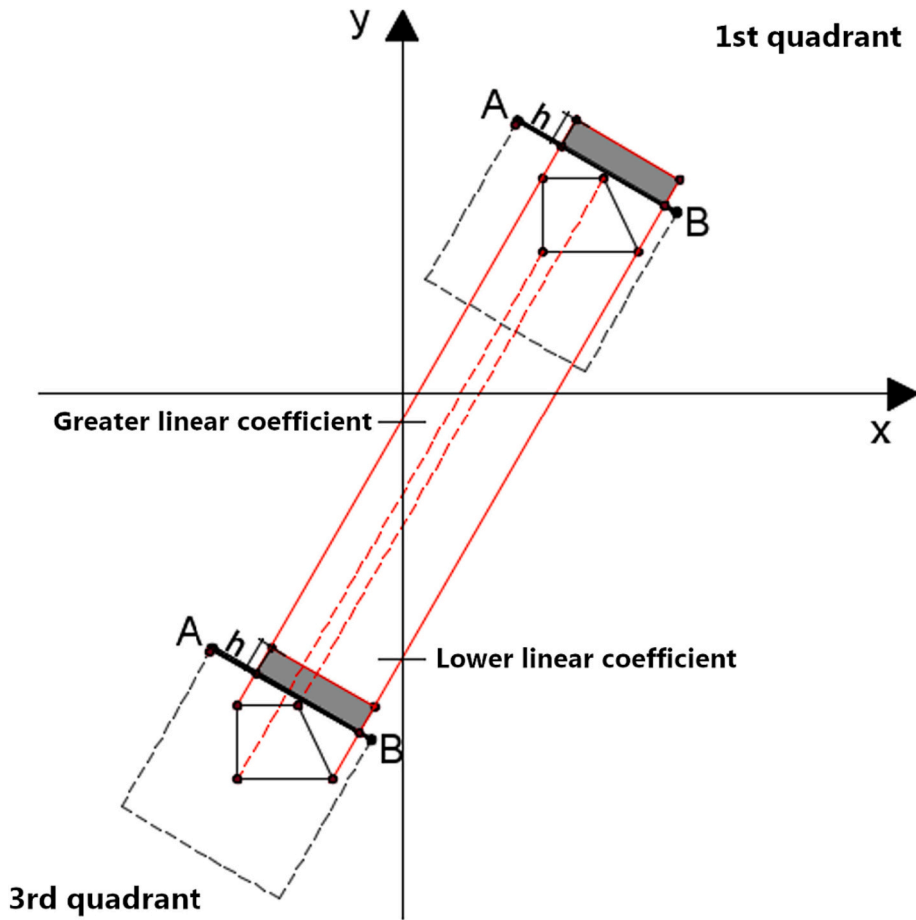


Fig. 7. Building frontal area projection – an example in the first and third quadrant.

n_{Base} is the projection base line linear coefficient.
 m_V is the vertex projection line angular coefficient.
 m_{Base} is the projection base line angular coefficient.

- Finding the y axis coordinate value by applying the resultant x axis coordinate value either to the projection base line equation or to the vertex projection line equation (see Appendix, Table A.5 and Table A.6)
- With h as the building height in meters, and (x_0, y_0) as the coordinates of the building vertex projection over the base line, the coordinates of the points that delimit the building height can be discovered using equation systems 2 and 3.

$$\begin{cases} x_h = x_0 + \text{sen}\theta * h \\ y_h = y_0 + \text{cos}\theta * h \end{cases} \quad (2)$$

$$\begin{cases} x_h = x_0 - \text{sen}\theta * h \\ y_h = y_0 + \text{cos}\theta * h \end{cases} \quad (3)$$

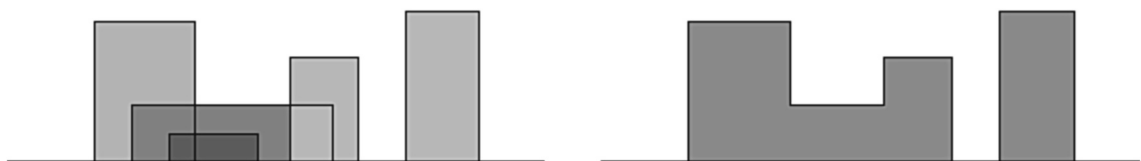


Fig. 8. Frontal area projection of buildings: on the left, each building is represented by a polygon; on the right, the polygons were merged.

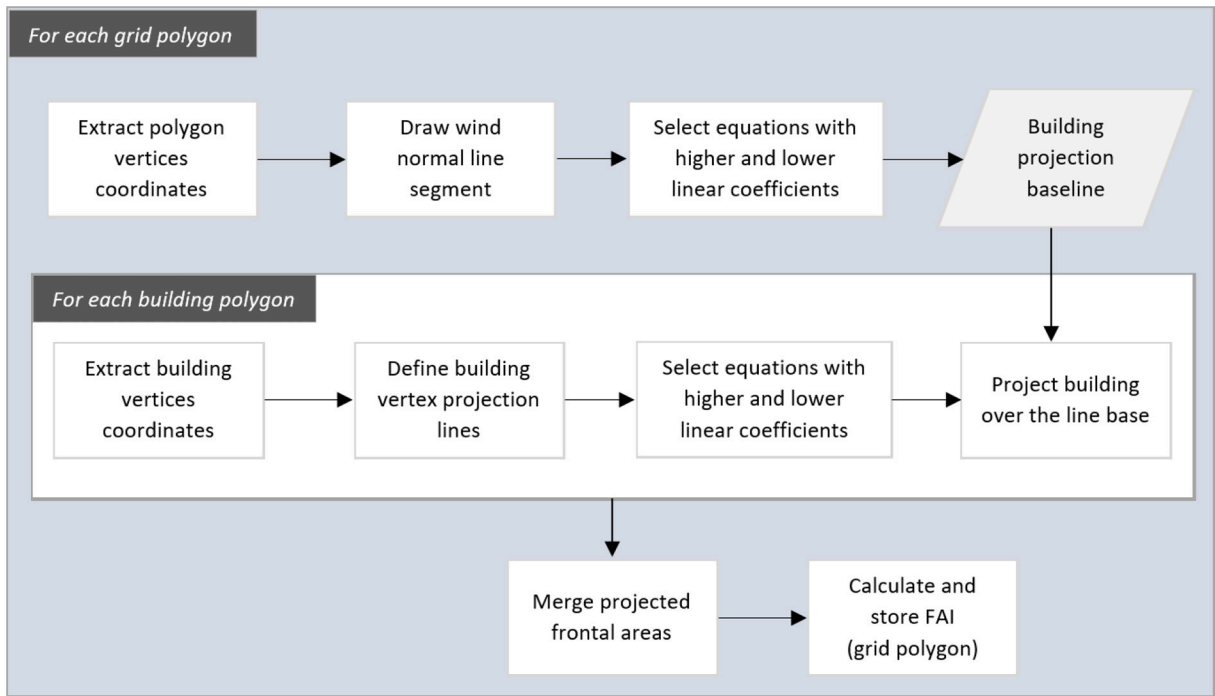


Fig. 9. FAI calculation for grid polygons.

2.3.5. Calculate FAI and generate map

After performing the frontal area projection of all buildings within a grid polygon, these multiple polygons are merged with GIS geoprocessing tools, creating a unique multipart polygon for each grid polygon (Fig. 8). This merge prevents the occurrence of overlapped projected areas. Then, the FAI of each grid polygon can be calculated according to Eq. (4) and following the steps of the diagram of Fig. 9.

$$\lambda_{f(\theta)} = \frac{A_{proj}(\theta)}{A_T} \quad (4)$$

Where:

θ is the considered wind direction angle.

$\lambda_{f(\theta)}$ is the FAI for a particular wind direction angle θ .

$A_{proj}(\theta)$ is the frontal area (without overlaps) of all buildings within a grid polygon for a particular wind direction angle θ .

A_T is the area of the grid polygon.

A FAI value is calculated and designated for each polygon of the calculation grid which, at this point, is a polygon feature layer. Then, with a GIS geoprocessing tool, this polygon grid with FAI values associated generates a FAI map raster image where the pixel has the same size as the calculation grid polygon.

2.4. Mapping the Thermal Potential Index

To generate the Thermal Potential Index (TPI) map (Fig. 10), the algorithm requires two keys inputs: (i) the calculation polygon grid layer and (ii) the thermal potential feature layer. This feature layer encompasses polygons outlining the ground surfaces within the chosen areas, as specified by the user. Furthermore, if weights have been assigned to distinct ground cover surfaces, a third optional input is available. This input enables the specification of the field name within the attribute table of the thermal potential feature layer, where these weights are adequately stored.

The first step, called the “thermal potential feature layer adjustment,” involves splitting any thermal potential polygon that overlaps multiple grid cell polygons. For each grid polygon, the individual materials' thermal potential is calculated as the product of its area, thermal mode, and weight (if applicable). These individual material thermal potentials are then summed, and the result is divided by the area of the grid polygon (Fig. 11).

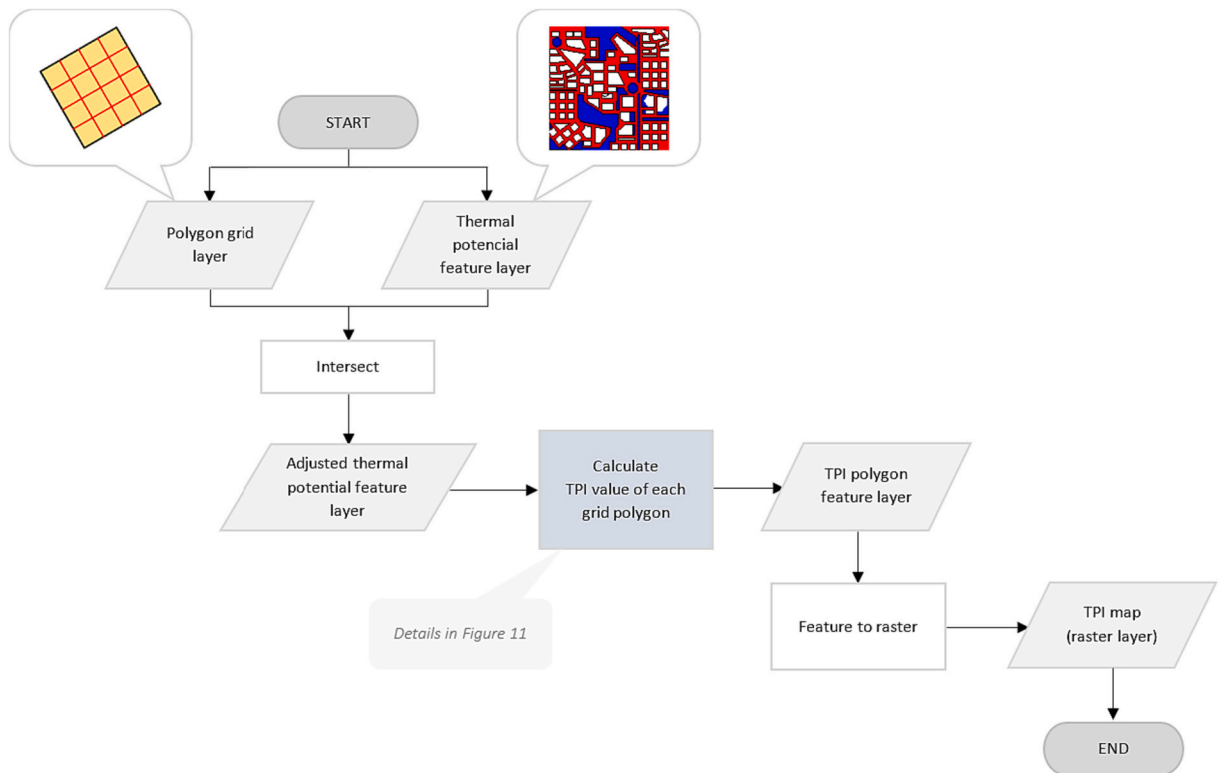


Fig. 10. TPI mapping process diagram.

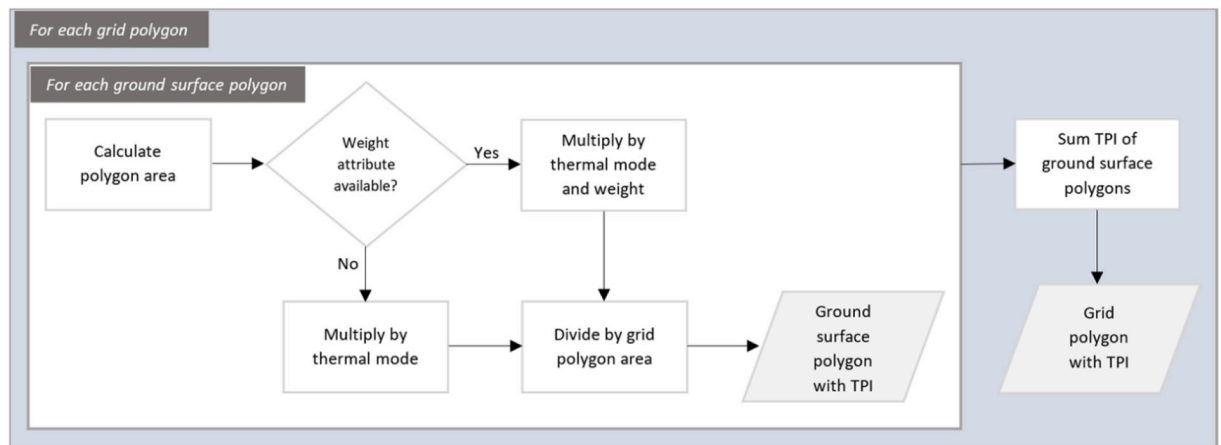


Fig. 11. Calculate Frontal Area Index of grid polygons.

Subsequently, the polygon grid with TPI values is converted to a raster, utilizing a spatial resolution equal to the calculation grid polygon dimensions. Finally, the generated raster layer is utilized to produce a TPI Map, effectively visualizing the thermal potential distribution across the study area.

2.5. Testing the algorithms

To test the algorithm developed in this research and implemented as ArcGIS Pro scrip tools, FAI and TPI maps are created concerning an urban area from São Paulo/ Brazil downtown (Fig. 12). The model is set up to create a 25 m × 25 m calculation grid cell regarding a 90° wind direction and no TPI weighted values are used.

According to the FAI calculation algorithm's logic, higher FAI values are expected in the regions of the map that show higher built

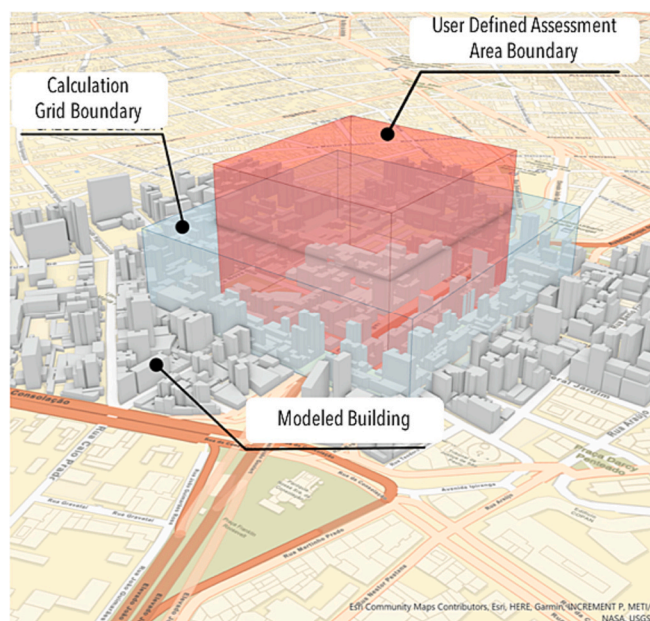


Fig. 12. ArcGIS Pro script tool testing Scenario. In red: the area delimited to be considered in the analysis. In gray: the expanded area to fit the desired grid cell size and wind angle direction. (For interpretation of the references to colour in this figure legend, the reader is referred to the web version of this article.)

density, considering the buildings' height and footprint. Regarding the TPI calculations, negative values are expected in the regions of the map predominantly covered with cooling groundcover materials and higher positive values are expected in regions with predominantly heating groundcover materials.

Considering the generated FAI map as a cost to the wind flow, a Least Cost Path (LCP) analysis is performed. Ten routes' starting and end points are evenly distributed in the windward and leeward map borders. The LCP analysis is performed using the ArcGIS Least Cost Path (Intelligence) tool from the embedded ArcGIS Intelligence toolbox.

3. Results and discussion

3.1. Frontal Area Index Map

Fig. 13 shows the resultant FAI map. The FAI values, for the considered urban area, range from 0.0 to 2.6. The road areas show FAI equal or close to zero, depending on whether the calculation grid cell covers a completely unbuilt or partially built region. The same applies to the other open or green spaces. The more densely built and verticalized regions show the highest FAI values.

As previously mentioned, the FAI considers the ground surface and buildings within a calculation grid cell. Therefore, the resultant FAI map precision is related to the grid cell size (J. Yang et al., 2019). However, smaller cell sizes increase the mapping computational costs. Therefore, the users must evaluate their needs and computational resources to choose the calculation grid configuration that best suits their purposes.

The algorithms presented in this research calculates the FAI by deducting possible duplicated areas caused by the overlap of buildings' projection areas. This approach is also used in research conducted by Wong et al. (2010), where the method to identify the overlapping areas to be disregarded was given by projecting a series of wind direction parallel lines and relating them to whether they reach the building facets. In the present research, the duplicated areas are removed by using ArcGIS geoprocessing tools to merge the projected area polygons. The duplication of projected areas is considered within the calculation cell level. Therefore, the model disregards possible impacts of this kind among buildings from different grid cells. This limitation is also shown by previous studies and may reflect in FAI value variations between mapping processes that consider different calculation grid cell dimensions or positions on the urban fabric. To mitigate this impact an FAI mapping approach was proposed (Wang and Ng, 2018) which, in short, consists of placing the calculation grid in different positions, generating multiple FAI maps and adding them into a single final map. This approach could be easily performed using the algorithm and ArcGIS script tool proposed in the present research.

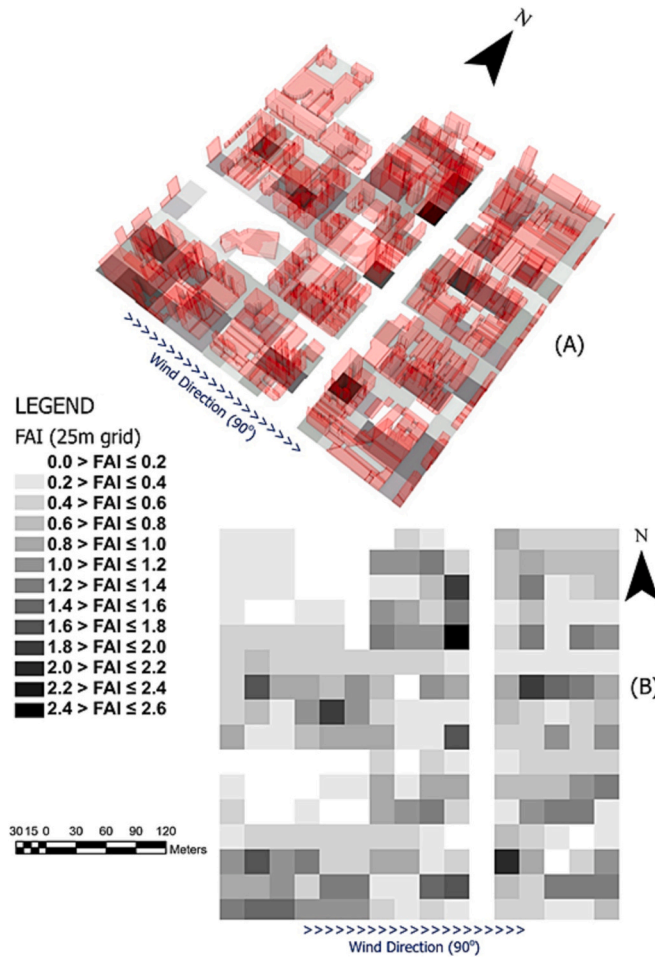


Fig. 13. Resultant FAI Map. (A) 3D building model superimposed over the FAI map; (B) 2D FAI map.

3.2. Thermal Potential Index Map

Fig. 14 shows the resultant TPI map. TPI values follow between -1 and 1.2 . The negative values indicate areas with a cooling potential, such as parks and vegetated areas, while positive values indicate heating potential which, in this case, represent paved roads. The TPI map shows coherence with the considered urban scenario.

The presented TPI calculation algorithm is similar to the calculation method proposed by Hsieh and Huang (2016). This differs by computing the value of an index, instead of considering only the area values, and by allowing the user to add weighted values to the different ground cover surface materials. Another example highlighting the usefulness of adding weights is when considering shaded and sunlit areas with the same cover material. These areas can be distinctly defined in the ground cover surfaces input layer. Subsequently, weight values can be assigned to these areas to incorporate the difference in thermal potential into the calculation process.

3.3. Predicting wind routes with the FAI map and LCP analysis

Fig. 15 shows the result of an LCP analysis using the FAI map as the cost feature layer. Several authors use this approach to predict the most likely ventilation routes over the urban fabric (S. L. Chen et al., 2017; Guo et al., 2018; Hsieh and Huang, 2016; Peng et al., 2017; Wong et al., 2010; Wong et al., 2011). Stemming from the LCP starting points, seven wind routes arise and reach the two vegetated open spaces. In these areas, routes merge, giving rise to two wind routes that meet in the region that comprise a north south wide road. Then, six main wind routes stand out to reach the LCP ending point. The considered urban configuration allows the green open spaces benefits to be spread over other urban fabric regions, such as the north south road that, according to the TPI map, shows the higher heating potential.

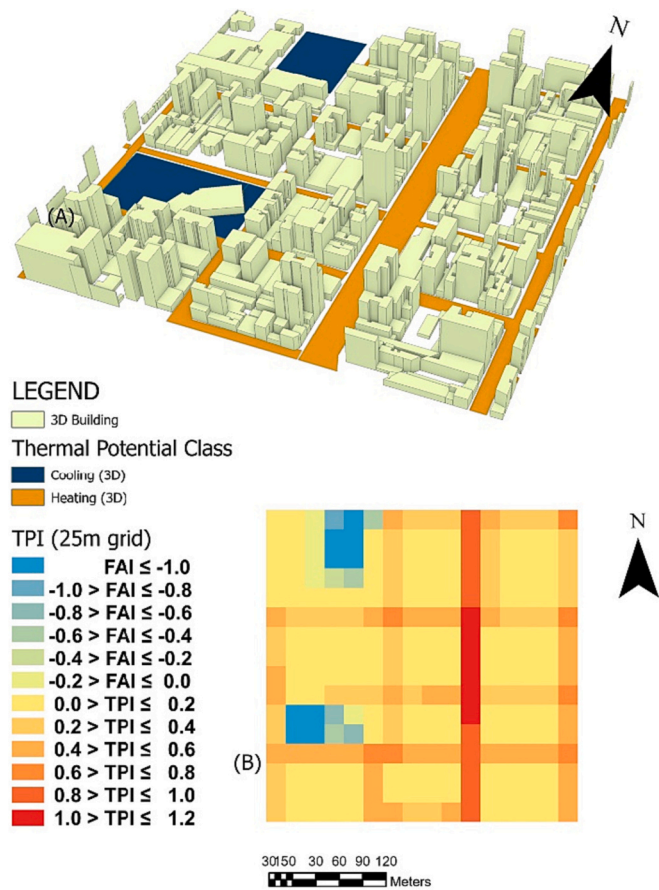


Fig. 14. Resultant TPI Map. (A) 3D building model superimposed over the TPI map; (B) 2D TPI map.

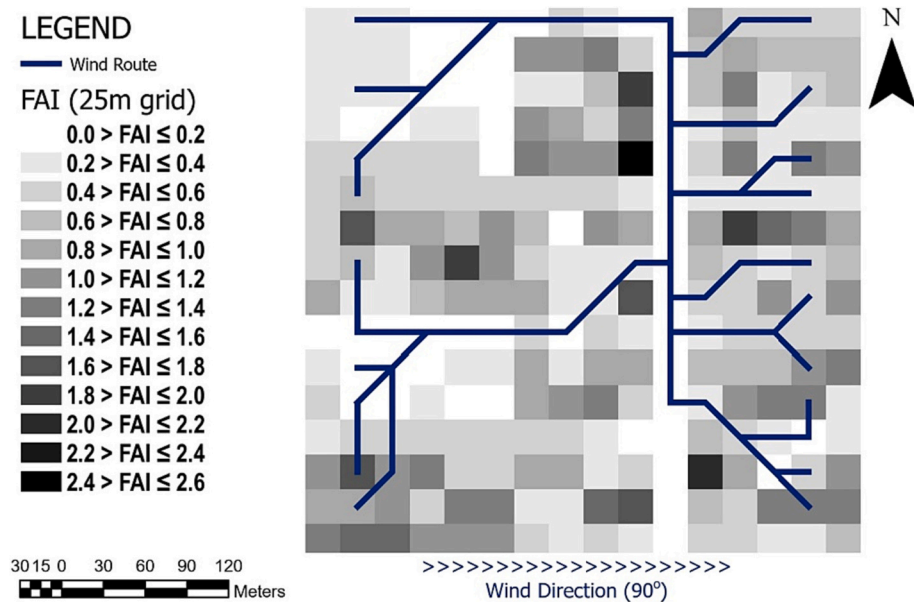


Fig. 15. Wind route predicted with the FAI map and LCP analysis.

4. Conclusion

To stimulate and promote an urban planning process focused on climatological aspects, from its early stages, this research translates urban climatology knowledge into simple, practical and day-to-day design and urban management amenable use tools. Algorithms to automatize FAI and TPI mapping processes within ArcGIS Pro are presented in detail and implemented as Python script tools in an ArcGIS toolbox. The indexes (FAI and TPI) are based on methods that already exist in the scientific literature on urban climatology. Therefore, a number of other studies make use of analysis and mapping methods very similar to those applied here. However, these studies apply their analyses and mappings in a timely manner, considering specific regions and realities. The present research differs from the others by presenting a step-by-step guide of the automatization mapping algorithms, in addition to providing a ready-to-use ArcGIS toolbox.

The achievements of this research show scientific and social relevance. Presented algorithms and tools may be used by the scientific community for discoveries and case study assessments concerning the urban climatological field. Once these research findings allow for the replication, on a large scale, of important studies, a possible implication of its dissemination is the increase in assessments focused on the urban morphology and land cover surface influence over the urban thermal environment. Furthermore, the detailed description of the algorithms allows other researchers to implement them in other GIS platforms, in addition to the ArcGIS Pro. Moreover, the provided tools can be used to help urban planners and managers to elaborate and review urban projects in daily practical processes. Due to the practicality and simplicity of modelling and assessment execution, the developed tools can be easily used by planning professionals without demanding advanced scientific or coding skills. The described algorithm and implemented tools generate maps that allow planners to assess, simulate and compare different urban scenarios. Therefore, the tools developed here can support urban planners and managers in decision-making, for example, by defining directives, in master plans, establishing height gauges for buildings or the percentage of soil occupation by certain types of materials.

Although there are already methods that consider topographic elements (S. L. [Chen et al., 2017](#)) in calculating the FAI, the algorithms developed here for calculating the FAI are restricted to considering buildings. Future studies can be carried out in order to add new elements, such as the terrain topography, arboreal vegetation, etc. The TPI mapping method is limited to a simple and almost qualitative ground cover material characterizations. Future work can also be carried out to implement these TPI maps by introducing more complex equations. Furthermore, The FAI is limited in its ability to discern variations in the layout of buildings, as it calculates the density of the facade as an average value along the 3rd dimension. Consequently, the FAI may assign the same value to a cluster of closely positioned small buildings and a single tall building, even though their respective impacts on wind patterns would differ significantly. Hence, forthcoming research could focus on formulating other algorithms within GIS for computing and mapping diverse urban climate-related indicators (e.g. Sky View Factor and Plan Area Ratio, etc.). This would enable the assessment of FAI and TPI in conjunction with other indicator layers, providing urban planners and managers with even more comprehensive information to support their decision-making.

Funding source declaration

This study was financed in part by the Coordenação de Aperfeiçoamento de Pessoal de Nível Superior - Brazil (CAPES) - Finance Code 001; the Conselho Nacional de Desenvolvimento Científico e Tecnológico - Brazil (CNPq); and from the Centre for Territory, Environment and Construction - Portugal (CTAC).

CRedit authorship contribution statement

Ana Paula Oliveira Favretto: Conceptualization, Investigation, Methodology, Software, Visualization, Writing – original draft. **Léa Cristina Lucas de Souza:** Supervision, Validation, Writing – review & editing. **Daniel Souto Rodrigues:** Data curation, Methodology, Software, Validation, Writing – review & editing.

Declaration of competing interest

The authors declare that they have no known competing financial interests or personal relationships that could have appeared to influence the work reported in this paper.

Data availability

Data will be made available on request.

Appendix

Table A.1
Summary of input data.



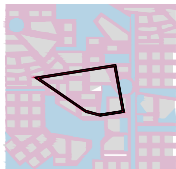
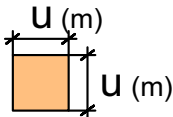
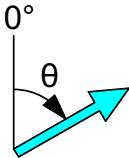
	Input data	Description
Buildings		<p>Polygon feature layer containing polygons that represent the building footprints.</p> <p>The building height has to be informed in meters at a column entitled 'H' (attribute table).</p> <p>Coordinate system: UTM.</p>
Ground Cover Surfaces		<p>Polygon feature layer containing polygon that represent the ground cover surface.</p> <p>The thermal potential class of each polygon has to be informed at a column entitled "THERMAL_MODE" (attribute table).</p>
Assessment Area Boundary		<p>Polygon Feature Layer containing a polygon delimiting the area to be analysed.</p>
Cell Size		<p>Value in meters</p>
Wind Direction		<p>Value in degrees, considering North = 0° increasing in clockwise direction</p>
Ground cover weight column name (optional)	Field in the attribute table	String value.

Table A.2
Calculation grid vertices equations for wind direction angles that are orthogonal to the Cartesian axis.

Vertex	x	y
V _{AB}	$x_C - r'$	$y_C + r'$
V _{BD}	$x_C + r'$	$y_C + r'$
V _{AE}	$x_C - r'$	$y_C - r'$
V _{DE}	$x_C + r'$	$y_C - r'$

Where:

x_C = centroid coordinate on the x-axis.

y_C = centroid coordinate on the y-axis.

r' = calculation grid inscribed circumference radius.

Table A.3
Calculation grid and inscribed circumference intersection point equations. These equations may be used for wind direction angles that are not orthogonal to the Cartesian axis.

Point	x	y
A	$x_C - \cos\theta' * r'$	$y_C + \sin\theta' * r'$
B	$x_C + \sin\theta' * r'$	$y_C + \cos\theta' * r'$
D	$x_C + \cos\theta' * r'$	$y_C - \sin\theta' * r'$
E	$x_C - \sin\theta' * r'$	$y_C - \cos\theta' * r'$

Where:

x_C = centroid coordinate on the x-axis.

y_C = centroid coordinate on the y-axis.

r' = calculation grid inscribed circumference radius.

θ' = wind direction angle reduced to the first quadrant.

Table A.4
Calculation grid border line equations.

Tangential points of contact	α value	Line equation
A	$\alpha_1 = 90^\circ - \theta'$	$y = \text{tg}(90^\circ - \theta') * x + y_A - \text{tg}(90^\circ - \theta') * x_A$
B	$\alpha_2 = 180^\circ - \theta'$	$y = \text{tg}(180^\circ - \theta') * x + y_B - \text{tg}(180^\circ - \theta') * x_B$
D	$\alpha_1 = 90^\circ - \theta'$	$y = \text{tg}(90^\circ - \theta') * x + y_D - \text{tg}(90^\circ - \theta') * x_D$
E	$\alpha_2 = 180^\circ - \theta'$	$y = \text{tg}(180^\circ - \theta') * x + y_E - \text{tg}(180^\circ - \theta') * x_E$

Where:

α_1 = angle between the x-axis and wind direction parallel lines.

α_2 = angle between the x-axis and wind direction perpendicular lines.

θ' = wind direction angle reduced to the first quadrant.

$x_A, y_A, x_B, y_B, x_D, y_D, x_E, y_E$ = coordinate x, y of the points A, B, D, and E, respectively

$$x_{AB} = \frac{y_B - \text{tg}(180^\circ - \theta')x_B - y_A + \text{tg}(90^\circ - \theta')x_A}{\text{tg}(90^\circ - \theta') - \text{tg}(180^\circ - \theta')} \tag{A.1}$$

$$x_{BD} = \frac{y_D - \text{tg}(90^\circ - \theta')x_D - y_B + \text{tg}(180^\circ - \theta')x_B}{\text{tg}(180^\circ - \theta') - \text{tg}(90^\circ - \theta')} \tag{A.2}$$

$$x_{AE} = \frac{y_E - \text{tg}(180^\circ - \theta')x_E - y_A + \text{tg}(90^\circ - \theta')x_A}{\text{tg}(90^\circ - \theta') - \text{tg}(180^\circ - \theta')} \tag{A.3}$$

$$x_{DE} = \frac{y_E - \text{tg}(180^\circ - \theta')x_E - y_D + \text{tg}(90^\circ - \theta')x_D}{\text{tg}(90^\circ - \theta') - \text{tg}(180^\circ - \theta')} \tag{A.4}$$

Where:

x_{AB} = coordinate of line A and line B intersection point

x_{BD} = coordinate of line B and line D intersection point

x_{DE} = coordinate of line D and line E intersection point

x_{AE} = coordinate of line A and line E intersection point

y_A, y_B, y_D and y_E = points A, B, D and E y-axis coordinate
 x_A, x_B, x_D and x_E = points A, B, D and E x-axis coordinate
 θ = wind direction angle reduced to the first quadrant.

Table A.5

Variables to automate the buildings' projection base line equation definition.

Quadrant	α_2	Angular coefficient (m_{Base})	Linear coefficient (n_{Base})	Line equation
Q. I	$180^\circ - \theta$	$tg\alpha_2$	$y_A - tg\alpha_2 \cdot x_A$	$y = m_{Base}x + n_{Base}$
Q. II	$180^\circ - \theta$			
Q. III	$360^\circ - \theta$			
Q. IV	$360^\circ - \theta$			

Where:

 α_2 = angle between the x-axis and wind direction perpendicular lines.**Table A.6**

Variables to automate the buildings' vertices projection line equation definition.

Quadrant	α_1	Angular coefficient (m_v)	Linear coefficient (n_v)	Line equation
Q. I	$90^\circ - \theta$	$tg\alpha_1$	$y_v - m_v x_v$	$y = m_v x + n_v$
Q. II	$270^\circ - \theta$			
Q. III	$270^\circ - \theta$			
Q. IV	$450^\circ - \theta$			

Where:

 α_1 = angle between the x-axis and wind direction parallel lines.

References

- Acerro, J.A., González-Asensio, B., 2018. Influence of vegetation on the morning land surface temperature in a tropical humid urban area. *Urban Clim.* 26, 231–243. <https://doi.org/10.1016/J.UCLIM.2018.09.004>.
- Alchapar, N.L., Pezzuto, C.C., Correa, E.N., Chebel Labaki, L., 2017. The impact of different cooling strategies on urban air temperatures: the cases of Campinas, Brazil and Mendoza, Argentina. *Theor. Appl. Climatol.* 130 (1–2), 35–50. <https://doi.org/10.1007/s00704-016-1851-5>.
- Arifwidodo, S.D., Chandrasiri, O., 2020. Urban heat stress and human health in Bangkok, Thailand. *Environ. Res.* 185 (November 2019), 109398 <https://doi.org/10.1016/j.envres.2020.109398>.
- Arnfield, A.J., 2003. Two decades of urban climate research: a review of turbulence, exchanges of energy and water, and the urban heat island. *Int. J. Climatol.* 23 (1), 1–26. <https://doi.org/10.1002/joc.859>.
- Back, Y., Kumar, P., Bach, P.M., Rauch, W., Kleidorfer, M., 2023. Integrating CFD-GIS modelling to refine urban heat and thermal comfort assessment. *Sci. Total Environ.* 858, 159729 <https://doi.org/10.1016/j.scitotenv.2022.159729>.
- Banerjee, S., Ching, N.Y., Yik, S.K., Dzyuban, Y., Crank, P.J., Pek Xin Yi, R., Chow, W.T.L., 2022. Analysing impacts of urban morphological variables and density on outdoor microclimate for tropical cities: a review and a framework proposal for future research directions. *Build. Environ.* 225 (September) <https://doi.org/10.1016/j.buildenv.2022.109646>.
- Chen, L., Ng, E., 2011. Quantitative urban climate mapping based on a geographical database: a simulation approach using Hong Kong as a case study. *Int. J. Appl. Earth Obs. Geoinf.* 13 (4), 586–594. <https://doi.org/10.1016/j.jag.2011.03.003>.
- Chen, S.L., Lu, J., Yu, W.W., 2017. A quantitative method to detect the ventilation paths in a mountainous urban city for urban planning: a case study in Guizhou, China. *Indoor Built Environ.* 26 (3), 422–437. <https://doi.org/10.1177/1420326X15626233>.
- Chen, S., Wong, N.H., Zhang, W., Ignatius, M., 2023. The impact of urban morphology on the spatiotemporal dimension of estate-level air temperature: A case study in the tropics. *Build. Environ.* 228, 109843. <https://doi.org/10.1016/j.buildenv.2022.109843>.
- Deschenes, O., 2014. Temperature, human health, and adaptation: a review of the empirical literature. *Energy Econ.* 46, 606–619. <https://doi.org/10.1016/j.eneco.2013.10.013>.
- Doan, Q.-V., Kusaka, H., Ho, Q.-B., 2016. Impact of future urbanization on temperature and thermal comfort index in a developing tropical city: Ho Chi Minh City. *Urban Clim.* 17, 20–31. <https://doi.org/10.1016/J.UCLIM.2016.04.003>.
- Doulos, L., Santamouris, M., Livada, I., 2004. Passive cooling of outdoor urban spaces. The role of materials. *Sol. Energy* 77 (2), 231–249. <https://doi.org/10.1016/J.SOLENER.2004.04.005>.
- Du, S., Zhang, X., Jin, X., Zhou, X., Shi, X., 2022. A review of multi-scale modelling, assessment, and improvement methods of the urban thermal and wind environment. *Build. Environ.* 213, 108860 <https://doi.org/10.1016/j.buildenv.2022.108860>.
- Fan, M., Chau, C.K., Chan, E.H.W., Jia, J., 2017. A decision support tool for evaluating the air quality and wind comfort induced by different opening configurations for buildings in canyons. *Sci. Total Environ.* 574, 569–582. <https://doi.org/10.1016/j.scitotenv.2016.09.083>.
- Faragallah, R.N., Ragheb, R.A., 2022. Evaluation of thermal comfort and urban heat island through cool paving materials using ENVI-Met. *Ain Shams Eng. J.* 13 (3), 101609 <https://doi.org/10.1016/j.asej.2021.10.004>.
- Gál, T., Unger, J., 2009. Detection of ventilation paths using high-resolution roughness parameter mapping in a large urban area. *Build. Environ.* 44 (1), 198–206. <https://doi.org/10.1016/j.buildenv.2008.02.008>.
- Georgescu, M., Morefield, P.E., Bierwagen, B.G., Weaver, C.P., 2014. Urban adaptation can roll back warming of emerging megapolitan regions. *Proc. Natl. Acad. Sci. U. S. A.* 111 (8), 2909–2914. <https://doi.org/10.1073/pnas.1322280111>.
- Guo, F., Schlindt, U., Wu, W., Hu, D., Sun, J., 2023. A new framework quantifying the effect of morphological features on urban temperatures. *Sustain. Cities Soc.* 99, 104923. <https://doi.org/10.1016/j.scs.2023.104923>.
- Guo, F., Zhang, H., Fan, Y., Zhu, P., Wang, S., Lu, X., Jin, Y., 2018. Detection and evaluation of a ventilation path in a mountainous city for a sea breeze: the case of Dalian. *Build. Environ.* 145, 177–195. <https://doi.org/10.1016/J.BUILDENV.2018.09.010>.

- Han, S., Hou, H., Estoque, R.C., Zheng, Y., Shen, C., Murayama, Y., Pan, J., Wang, B., Hu, T., 2023. Seasonal effects of urban morphology on land surface temperature in a three-dimensional perspective: A case study in Hangzhou, China. *Build. Environ.* 228, 109913. <https://doi.org/10.1016/j.buildenv.2022>.
- He, Y., Liu, Z., Ng, E., 2022. Parametrization of irregularity of urban morphologies for designing better pedestrian wind environment in high-density cities – a wind tunnel study. *Build. Environ.* 226 (August), 109692. <https://doi.org/10.1016/j.buildenv.2022.109692>.
- Hebbert, M., 2014. Climatology for city planning in historical perspective. *Urban Clim.* 10, 204–215. <https://doi.org/10.1016/j.uclim.2014.07.001>.
- Hebbert, M., Jankovic, V., 2013. Cities and climate change: the precedents and why they matter. *Urban Stud.* 50 (7), 1332–1347. <https://doi.org/10.1177/0042098013480970>.
- Hebbert, M., Mackillop, F., 2013. Urban climatology applied to urban planning: a postwar knowledge circulation failure. *Int. J. Urban Reg. Res.* 37 (5), 1542–1558. <https://doi.org/10.1111/1468-2427.12046>.
- Hsieh, C.-M., Huang, H.-C., 2016. Mitigating urban heat islands: a method to identify potential wind corridor for cooling and ventilation. *Comput. Environ. Urban Syst.* 57, 130–143. <https://doi.org/10.1016/j.compenvurbysys.2016.02.005>.
- Igun, E., Williams, M., 2018. Impact of urban land cover change on land surface temperature. *Glob. J. Environ. Sci. Manag.* 4 (1), 47–58. <https://doi.org/10.22034/gjesm.2018.04.01.005>.
- Jabareen, Y., 2015. City planning deficiencies & climate change – the situation in developed and developing cities. *Geoforum* 63, 40–43. <https://doi.org/10.1016/J.GEOFORUM.2015.05.017>.
- Kleerekoper, L., van Esch, M., Salcedo, T.B., 2012. How to make a city climate-proof, addressing the urban heat island effect. *Resour. Conserv. Recycl.* 64, 30–38. <https://doi.org/10.1016/j.resconrec.2011.06.004>.
- Kotharkar, R., Dongarsane, P., Keskar, R., 2023. Determining influence of urban morphology on air temperature and heat index with hourly emphasis. *Build. Environ.* 233, 110044. <https://doi.org/10.1016/j.buildenv.2023.110044>. ISSN 0360-1323.
- Kravchenko, J., Abernethy, A.P., Fawzy, M., Lyerly, H.K., 2013. Minimization of heatwave morbidity and mortality. *Am. J. Prev. Med.* 44 (3), 274–282. <https://doi.org/10.1016/j.amepre.2012.11.015>.
- Li, H., Li, Y., Wang, T., Wang, Z., Gao, M., Shen, H., 2021. Quantifying 3D building form effects on urban land surface temperature and modeling seasonal correlation patterns. *Build. Environ.* 204, 108132. <https://doi.org/10.1016/j.buildenv.2021.108132>.
- Li, J., You, W., Ding, W., 2022. Exploring urban space quantitative indicators associated with outdoor ventilation potential. *Sustain. Cities Soc.* 79 (January) <https://doi.org/10.1016/j.scs.2022.103696>.
- Lindberg, F., Grimmond, C.S.B., Gabey, A., Huang, B., Kent, C.W., Sun, T., Theeuwes, N.E., Järvi, L., Ward, H.C., Capel-Timms, I., Chang, Y., Jonsson, P., Krave, N., Liu, D., Meyer, D., Olofson, K.F.G., Tan, J., Wästberg, D., Xue, L., Zhang, Z., 2018. Urban Multi-scale Environmental Predictor (UMEP): an integrated tool for city-based climate services. *Environ. Model Softw.* 99, 70–87. <https://doi.org/10.1016/j.envsoft.2017.09.020>.
- Liu, Y., Xu, Y., Zhang, F., Shu, W., 2020. A preliminary study on the influence of Beijing urban spatial morphology on near-surface wind speed. *Urban Clim.* 34 (June), 100703. <https://doi.org/10.1016/j.uclim.2020.100703>.
- Liu, X., Huang, B., Li, R., Zhang, J., Gou, Q., Zhou, T., Huang, Z., 2022. Wind environment assessment and planning of urban natural ventilation corridors using GIS: Shenzhen as a case study. *Urban Clim.* 42, 101091. <https://doi.org/10.1016/j.uclim.2022.101091>.
- Marchetti, E., Capone, P., Freda, D., 2016. Climate change impact on microclimate of work environment related to occupational health and productivity. *Ann. Ist. Super. Sanita* 52 (3), 338–342. https://doi.org/10.4415/ANN_16_03_05.
- McGeehin, M., Mirabelli, M., 2001. The potential impacts of climate variability and change on temperature-related morbidity and mortality in the United States. *Environ. Health Perspect.* 109 (Suppl(May)), 185–189. <https://doi.org/10.2307/3435008>.
- Mills, G., 2014. Urban climatology: history, status and prospects. *Urban Clim.* 10, 479–489. <https://doi.org/10.1016/J.UCLIM.2014.06.004>.
- Moazzam, M.F.U., Doh, Y.H., Lee, B.G., 2022. Impact of urbanization on land surface temperature and surface urban heat island using optical remote sensing data: a case study of Jeju Island, Republic of Korea. *Build. Environ.* 222, 109368. <https://doi.org/10.1016/j.buildenv.2022.109368>.
- Nakata-Osaki, C.M., Souza, L.C.L., Rodrigues, D.S., 2018. THIS – Tool for Heat Island Simulation: a GIS extension model to calculate urban heat island intensity based on urban geometry. *Comput. Environ. Urban Syst.* 67 (July 2016), 157–168. <https://doi.org/10.1016/j.compenvurbysys.2017.09.007>.
- Omonijo, A.G., 2017. Assessing seasonal variations in urban thermal comfort and potential health risks using Physiologically Equivalent Temperature: a case of Ibadan, Nigeria. *Urban Clim.* 21, 87–105. <https://doi.org/10.1016/j.uclim.2017.05.006>.
- Palusci, O., Monti, P., Cecere, C., Montazeri, H., Blocken, B., 2022. Impact of morphological parameters on urban ventilation in compact cities: the case of the Tuscolano-Don Bosco district in Rome. *Sci. Total Environ.* 807, 150490. <https://doi.org/10.1016/j.scitotenv.2021.150490>.
- Paz, S., Negev, M., Clermont, A., Green, M.S., 2016. Health aspects of climate change in cities with Mediterranean climate, and local adaptation plans. *Int. J. Environ. Res. Public Health* 13 (4). <https://doi.org/10.3390/ijerph13040438>.
- Peng, F., Wong, M.S., Wan, Y., Nichol, J.E., 2017. Modeling of urban wind ventilation using high resolution airborne LiDAR data. *Comput. Environ. Urban Syst.* 64, 81–90. <https://doi.org/10.1016/J.COMPENVURBSYS.2017.01.003>.
- Ren, C., Lau, K.L., Yiu, K.P., Ng, E., 2013. The application of urban climatic mapping to the urban planning of high-density cities: the case of Kaohsiung, Taiwan. *Cities* 31, 1–16. <https://doi.org/10.1016/J.CITIES.2012.12.005>.
- Saaroni, H., Ben-Dor, E., Bitan, A., Potchter, O., 2000. Spatial distribution and microscale characteristics of the urban heat island in Tel-Aviv, Israel. *Landsc. Urban Plan.* 48 (1–2), 1–18. [https://doi.org/10.1016/S0169-2046\(99\)00075-4](https://doi.org/10.1016/S0169-2046(99)00075-4).
- Shi, Y., Zhang, Y., 2022. Urban morphological indicators of urban heat and moisture islands under various sky conditions in a humid subtropical region. *Build. Environ.* 214, 108906. <https://doi.org/10.1016/j.buildenv.2022.108906>.
- Smith, I.A., Fabian, M.P., Hutyrá, L.R., 2023. Urban green space and albedo impacts on surface temperature across seven United States cities. *Sci. Total Environ.* 857, 159663. <https://doi.org/10.1016/j.scitotenv.2022.159663>.
- Touati, N., Gardes, T., Hidalgo, J., 2020. A GIS plugin to model the near surface air temperature from urban meteorological networks. *Urban Clim.* 34, 100692. <https://doi.org/10.1016/j.uclim.2020.100692>.
- Tun, K., Mg, T., (2020). Temperature reduction in urban surface materials through tree shading depends on surface type not tree species. *Forests* (11, 11). doi:<https://doi.org/10.3390/f11111141>.
- Wang, W., Ng, E., 2018. Air ventilation assessment under unstable atmospheric stratification — a comparative study for Hong Kong. *Build. Environ.* 130, 1–13. <https://doi.org/10.1016/j.buildenv.2017.12.018>.
- Wong, M.S., Nichol, J.E., To, P. H., Wang, J., 2010. A simple method for designation of urban ventilation corridors and its application to urban heat island analysis. *Build. Environ.* 45 (8), 1880–1889. <https://doi.org/10.1016/j.buildenv.2010.02.019>.
- Wong, M.S., Nichol, J., Ng, E., 2011. A study of the “wall effect” caused by proliferation of high-rise buildings using GIS techniques. *Landsc. Urban Plan.* 102 (4), 245–253. <https://doi.org/10.1016/j.landurbplan.2011.05.003>.
- Wright, C.Y., Garland, R.M., Norval, M., Vogel, C., 2014. Human health impacts in a changing South African climate. *S. Afr. Med. J.* 104 (8), 579–582. <https://doi.org/10.7196/SAMJ.8603>.
- Yang, J., Wang, Y., Xiao, X., Jin, C., Xia, J. (Cecilia), Li, X., 2019. Spatial differentiation of urban wind and thermal environment in different grid sizes. *Urban Clim.* 28. <https://doi.org/10.1016/j.uclim.2019.100458>.
- Xu, D., Zhou, D., Wang, Y., Xu, W., Yang, Y., 2019. Field measurement study on the impacts of urban spatial indicators on urban climate in a Chinese basin and static-wind city. *Build. Environ.* 147. <https://doi.org/10.1016/j.buildenv.2018.10.042>.
- Yang, Z., Chen, Y., Wu, Z., 2021a. How urban expansion affects the thermal environment? A study of the impact of natural cities on the thermal field value and footprint of thermal environment. *Ecol. Indic.* 126, 107632. <https://doi.org/10.1016/j.ecolind.2021.107632>.

- Yang, J., Yang, Y., Sun, D., Jin, C., Xiao, X., 2021b. Influence of urban morphological characteristics on thermal environment. *Sustain. Cities Soc.* 72 (March) <https://doi.org/10.1016/j.scs.2021.103045>.
- Yao-Dong, D., Xian-Wei, W., Xiao-Feng, Y., Wen-Jun, M., Hui, A., Xiao-Xuan, W., 2013. Impacts of climate change on human health and adaptation strategies in South China. *Adv. Clim. Chang. Res.* 4 (4), 208–214. <https://doi.org/10.3724/SP.J.1248.2013.208>.
- Yin, S., Liu, J., Han, Z., 2022. Relationship between urban morphology and land surface temperature—A case study of Nanjing City. *PLOS ONE* 17. <https://doi.org/10.1371/journal.pone.0260205>.
- Yuan, C., Adelia, A.S., Mei, S., He, W., Li, X., Norford, L., 2020. Mitigating intensity of urban heat island by better understanding on urban morphology and anthropogenic heat dispersion. *Build. Environ.* 176, 106876. <https://doi.org/10.1016/j.buildenv.2020.106876>.
- Zhang, J., Li, Z., Hu, D., 2022. Effects of urban morphology on thermal comfort at the micro-scale. *Sustain. Cities Soc.* 86, 104150. <https://doi.org/10.1016/j.scs.2022.104150>.
- Zhang, B., Li, G., Ma, Y., Pan, X., 2018. Projection of temperature-related mortality due to cardiovascular disease in Beijing under different climate change, population, and adaptation scenarios. *Environ. Res.* 162 (December 2017), 152–159. <https://doi.org/10.1016/j.envres.2017.12.027>.